Data Driven Forecast of Concurrent Flame Spread in Micro-Gravity

Xiuqi Xi[a] , José L. Torero[a] and Augustin Guibaud [a]

[a] *University College London, London WC1E 6BT, UK*

Abstract

This paper presents a methodology that combines data assimilation and physical modelling of flame spread for fire growth forecast. The concurrent flame spreading over a flat solid sample in the absence of buoyant flows is considered as a simple canonical fire spread configuration. To predict flame spread rate and flame length evolution, the analytical solution to the two-dimensional boundary layer non-premixed combustion problem is combined with a CFD model which delivers the structure of the flow away from the fuel surface. In the process, two coefficients which intervene in the gas and solid heat transfer equations are assimilated using the pyrolysis length data as a flame spread rate surrogate input to absorb the shortcomings of the modelling. The robustness of the overall method is evaluated through convergence assessment of these two assimilated variables for different initial guesses, and for different values of the input invariants. Validation over large-scale microgravity data provides confidence in this approach, and demonstrates its potential to deliver flame spread predictions from initial measurements at a reduced computational cost. However, discrepancies between flame length measurements and predictions question the degree of correlation between pyrolysis and flame lengths.

Keywords: Data assimilation, concurrent flame spread, hybrid model, microgravity

Nomenclature

B	Spalding B number
C_1	The first assimilation variable for ignition delay time
C_2	The second assimilation variable for heat loss term at fuel surface[MJ/(kg·m$^{1/2}$)]
c_{pg}	Specific heat of the gas at constant pressure [J/(kgK)]
c_s	Specific heat of the solid [J/(kg·K)]
f	Similarity stream function
g	gravitational force [m/s^2]
J	Mixture fraction
k_g	Thermal conductivity of the gas [W/(m·K)]
k_s	Thermal conductivity of the solid [W/(m·K)]
L	Heat of gasification [J/kg]
$\dot{m}_{\mathrm{f}}''$	Mass loss rate [kg/(m^2·s)]
Pr	Prandtl number
$\dot{q}_{\mathrm{L}}''$	Total heat losses flux at the fuel surface [J/(kg·m^2·s)]
$\dot{q}_e''$	External heat flux [W/m^2]
$\dot{q}_{max}''$	Maximum heat flux of the preheat region [W/m^2]
Q	Total heat losses [J/kg]
Re	Reynolds number

s	Stoichiometric ratio
T_{ig}	Ignition temperature [K]
T_{∞}	Ambient temperature [K]
t_{ig}	Ignition time [s]
t_p	Pyrolysis time [s]
U_{∞}	Ambient velocity [m/s]
u	Streamwise velocity [m/s]
v_p	Pyrolysis velocity [m/s]
v	Transverse velocity [m/s]
x	Streamwise coordinate [m]
x_p	Pyrolysis length [m]
$Y_{o\infty}$	Ambient oxidizer fraction
y	Transverse coordinate [m]
Z	Schwab-Zeldovich variable
ΔH	Heat of combustion [J/kg]
ε	Convergence criteria
η	Similarity variable
δ_a	Thickness of the analytical described gas phase region [m]
δ_f	Preheat length [m]
ρ_s	Density of the solid [kg/m^3]
ν	Kinetic viscosity [m^2/s]

ψ	Stream function

1. Introduction

Safe and timely decisions in firefighting are essential to prevent life losses and minimize material damage. Although firefighting protocols are based on experience, there has been a clear recognition in the last two decades that predictions of fire growth can be of significant importance to support dynamic risk assessments when there is a need to deviate from these protocols [1]. It is therefore necessary to develop tools and procedures to deliver such predictions. Unfortunately, present tools are not precise enough, robust enough and, particularly, not fast enough to deliver adequate information in a timely manner [2]. Furthermore, even if these tools were to sufficiently improve, the large uncertainty regarding materials, configurations and geometries results in first principles predictions that will be inevitably inaccurate.

Most previous studies of fire spread are conducted over one- or two-dimensional condensed fuels, either liquid [3] or solid [4,5], and are classified as either concurrent or opposed flame spread. In concurrent flame spread, convective heat transfer is in the direction of spread and, therefore, it is considered as being a greater hazard than opposed flame spread, where convective heat transfer opposes the spread of the flame [6]. For this reason, this paper will focus on concurrent flame spread.

In concurrent flame spread, the spread rate is controlled by heat and mass transport coupled with combustion and pyrolysis chemical reactions. The processes involved can be divided into two loosely coupled sets of processes occurring in the gas and condensed phases. Such a loose coupling is possible because gas phase and condensed phase processes feature very different characteristic times[6]. Decoupling the fast reactive-flow from the slower pyrolyzing fuel thus makes it possible to treat the

two phases separately and allows to only consider interactions in an approximated manner through their respective domain boundaries. With a set of assumptions tailored to simplify the gas-phase equations, Emmons first provided an analytical solution for the mass loss rate at the fuel surface [7]. The flame spread over a thin fuel was then formulated by de Ris with additional models to account for the heat transfer to the condensed phase [8]. This model, and others that followed [9], assumed a quasi-steady approach for the gas phase. Within the flat fuel plate configuration, additional work managed to include the effects of chemistry [4,10], thermal thickness [11] and turbulence [12]. These analytical models provide means to calculate the flame spread rate as well as gas phase temperatures and flame lengths [13]. However, the quasi-steady-state assumption required for the boundary layer flow imposes severe limitations to the applicability of any of these models to real scenarios, where the flow evolves in a complex manner. Without a time-dependent description of the gas phase, the boundary conditions at the surface of the condensed phase, particularly the heat fluxes from the flame, are poorly evaluated. Moreover, assumptions associated with the analytical model further limit the precision of the predictions.

To account for a dynamic evolution, Computational Fluid Dynamic (CFD) models solve the various differential equations which describe the evolution of the gas phase in space and time. The generation, transport and consumption of mass, species, momentum, and energy are then modelled in discretised cells. Because equations are solved locally, a more detailed and precise description can be achieved. Many CFD studies for concurrent flame spread have appeared in the literatures in the last three decades, covering a range of objectives such as coupling of different phases [14], the effects of gravity [15] or the prediction of spread rates [16]. Yet, the computational time is governed by the mesh size, which in turn is controlled by both the required precision of gradients at the interface between

the gas and condensed phases and convergence requirements. In the concurrent flame spread configuration, these require exceptional mesh refinements since it is essentially a near-wall reactive flow driven by fuel mass transfer. Consequently, the computational resources imposed for predictions using numerical models are far beyond the capability of present computers when attempting to approach real-time forecasts of real-size fires. This undermines the potential of CFD simulations as an approach towards fire growth prediction. It is also important to highlight that numerical models need a significant number of parameters to absorb phenomena occurring at a sub-mesh scale: the validation of the choice of parameterization and quantification of these parameters then controls the quality of the predictions. Furthermore, the results can be especially sensitive to these input parameters because of inherent non-linearities in the system.

Atmospheric scientists faced similar issues more than 50 years ago [17]. To overcome them, it was proposed to continuously re-initialize predictions with updated measurements, which is known as data assimilation or data-driven prediction [18]. Data assimilation consists in updating the estimations of the true state of a real physical system by optimally incorporating observations with fluid dynamics models following a calibrated initial value approach [19]. This means that a forward predictive model is permanently corrected with the observations through inverse model procedures. Such methodology is utilized in the model the wildland fire spread[20,21]. In the field of fire safety, Cowlard et al. successfully corrected parameters in an analytical forward concurrent flame spread model using experimental observations such as flame length [1]. However, predictions with this configuration are limited to the pyrolysis and flame lengths, and the quality of the model still relies heavily on strong steady spread assumptions related to the analytical model of the gas phase. This limits the range of application of this model.

In order to combine the benefits of analytical and CFD modelling, and to improve on the quality of the prediction using data assimilation, a data-driven hybrid model has already been successfully derived for the droplet combustion system [22]. A steady-state analytical gas phase model adequately describes the heat and mass transfer at the fuel surface, providing self-similar fields of velocity, temperature, and species in the vicinity of the droplet. A numerical description of the gas-phase flow and kinetics then computes at a refined scale the properties of the reactive flow away from the surface, with a drastic reduction in the computational cost compared to an all-numerical model where refined meshing is needed in the near-wall region. The dynamic heat flux distribution at the fuel surface is extracted from the CFD model and is then integrated to an analytical model in the condensed phase. This provides the required time-dependant pyrolysis rate feedback into the analytical model of the gas phase. Data assimilation is then carried out to adjust the most important physical parameters capturing the condensed phase and gas phase interactions, and thus absorb the inherent parametric uncertainties. This hybrid configuration benefits from the precision of the CFD and analytical models at a reduced computational cost.

In the present study, the work of Xi et al. [22] is extended to the two-dimensional situation of concurrent flame spread over a flat surface. The analytical and numerical models implemented over the flat fuel sample are described first, together with the boundary conditions through which information is transferred. The precision of the hybrid model is then evaluated against experimental observations of flame spread over a large flat sample of thick Polymethyl Methacrylate (PMMA) conducted in microgravity conditions. Although a pure forced flow can only occur in microgravity, reduced pressure can be used approximately to replicate flame behaviour of normal gravity conditions[23]. The model is then used to predict concurrent flame spread at a reduced computational

time.

2. Hybrid data-driven Concurrent Flame Spread Model

A two-dimensional (2D) hybrid model for simulating concurrent flame spread is proposed to combine the benefits of CFD and analytical modelling and to obtain precise predictions at low computational cost. As illustrated in Figure 1, analytical models are proposed for the condensed fuel phase and in a thin gas region in the vicinity of the fuel surface, while a CFD model is implemented away from the fuel surface. The condensed phase is assumed to be a solid of infinite thickness. The analytically described gas phase region at the fuel surface should be thin enough to leave the reaction zone above the preheated fuel in the CFD region, and thick enough to enable an analytical solution for species concentration, flow velocity, and temperature in the viscous boundary layer, consequently reducing the computational time. The thickness in the orthogonal coordinate y (perpendicular to the fuel surface) is case-specific, and its calculation needs a detailed definition. Nevertheless, simple scaling analysis performed in Section 3.2 will indicate that it is of the order of a few millimetres.

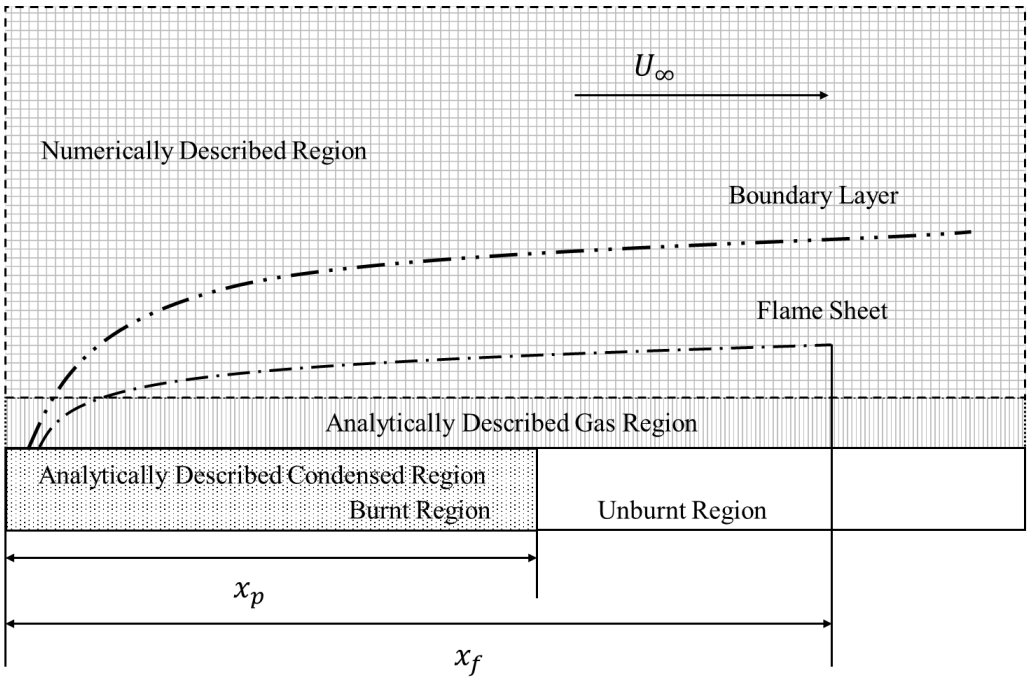

Figure 1 Schematic diagram of the different regions solved in the hybrid model for concurrent

flame spread. The condensed region is treated analytically, while the gas-phase is a combination of an analytical domain at the solid surface and a numerical CFD domain.

2.1 Analytical Model for the Gas Phase Region

Gas phase region of concurrent laminar flame spread in a boundary layer flow has been described analytically following different sets of heat and mass transfer hypotheses[7,24,25]. Assuming: 1) a steady laminar flow, 2) infinitely fast chemistry, 3) equal mass, momentum, and heat diffusion coefficients, 4) $\rho\mu = constant$ with ρ the gas-phase density and μ its dynamic viscosity, and 5) neglecting radiative heat transfer, the energy and species conservation equations can be expressed with the Schwab-Zeldovich variables Z_i. The purely forced convective flow can be described by

$$f''' + ff'' = 0 \tag{1}$$

with $f = \psi / \left(x / Re\right)^{1/2}$, where ψ is the stream function, x is the streamwise coordinate, and Re is the Reynolds number. The associated energy-species equation coupled with the momentum equation is

$$J'' + PrfJ' = 0 \tag{2}$$

where Pr is the Prandtl number, and J the mixture fraction defined as $J = \left(Z_i - Z_{i,w}\right) / \left(Z_{i.\infty} - Z_{i,w}\right)$, where the indexes w, ∞ correspond to locations near and away from the fuel surface, respectively. The boundary conditions are

$$\begin{array}{lll} f'(0) = 0 & f'(\infty) = 2 & f(0) = BJ'(0)/Pr \\ J(0) = 1 & & J(\infty) = 0 \end{array} \tag{3}$$

In these equations, η is the self-similar variable and the mass transfer (or Spalding) number B is

$$B = \frac{\Delta H Y_{o\infty} s - c_{pg}(T_{ig} - T_\infty)}{L + Q} \tag{4}$$

where ΔH is the heat of combustion, $Y_{o,\infty}$ is the ambient oxygen content, s is the stoichiometric

oxidizer-fuel mass ratio, c_{pg} is the specific heat capacity of the gas, T_{ig} is the ignition temperature of the fuel, T_∞ is the ambient temperature, L is the heat of gasification and Q is defined as

$$Q = \frac{\dot{q}''_{\mathrm{L}}}{\dot{m}''_{\mathrm{f}}} \tag{5}$$

where $\dot{q}''_{\mathrm{L}}$ represents the net non-convective heat transfer at the fuel surface (generally referred to as net losses) and $\dot{m}''_{\mathrm{f}}$ is the fuel mass flux at the surface. Q is then a function of the streamwise coordinate x. Ultimately, the Spalding B number represents the relative importance of different heat transfer modes during steady-state burning and has been demonstrated to be an effective parameter to characterize flammability. Furthermore, Emmons showed that, given the different characteristic time scales of solid and gas phase processes, the gas phase attains steady state much faster than the solid and therefore this approach can be used as a quasi-steady mean to assess concurrent flame spread.

The exact solutions to the above equations require numerical iterations. Polynomial approximations can be used to obtain the two-dimensional profiles of the mixture fractions and the velocity, as specified in [24,26]. Moreover, the inverse Howarth-Dorodnitsyn transformation is necessary to account for density variations. For the purpose of this study, a linear density profile is assumed, following Baum *et al*. [27].

2.2 Analytical Model for the Condensed Region

The flame spread rate v_p can be defined as the progression of the pyrolysis region. For the pyrolysis front located at $x = x_p$ to progress, the non-burning condensed phase must be heated to a point where it releases sufficient fuel in the gas to ignite.

$$v_p = \frac{dx_p}{dt} = \frac{\delta_f}{t_{ig}} \tag{6}$$

with δ_f the preheat length and t_{ig} the characteristic time to ignite the virgin fuel. The ignition time

t_{ig} is the sum of the time t_p for the combustible material to reach the pyrolysis temperature and the time t_g for the fuel volatiles to attain the lean flammability limit. An induction time associated to the onset of the reaction chemistry might be necessary, but induction time generally is much smaller that the two other characteristic timescales in the presence of a pilot flame, and will thus be neglected here. In addition, for the concurrent flame spread under fast chemical kinetic conditions, it can also be assumed that $t_p >> t_g$, hence t_{ig} is approximated as t_p [28]. A final assumption requires the fuel supply to be large enough so that when the lean flammability limit is attained and the onset of combustion takes place, that the reaction chemistry is very fast. This means that the flame is burning far from quenching or blow-off conditions [29].

For a thermally thick material and sufficiently high external heat supply, the pyrolysis time is found by solving the one-dimensional transient heat conduction equations in the solid material. With the semi-infinite boundary condition at the back, the ignition time can be established as [30]:

$$t_{ig} = t_p = \frac{\pi}{4} k_s \rho_s c_s \left(\frac{T_{ig} - T_\infty}{\dot{q}''_e} \right)^2 \tag{7}$$

where $k_s \rho_s c_s$ is the thermal inertia of the material, T_{ig} is the pyrolysis temperature, and $\dot{q}''_e$ is the external heat flux. An external heat flux of 11 kW/m² has been experimentally identified as the critical value below which PMMA cannot ignite [31]. As such, this equation will only be considered for fluxes above this critical value. In the studied configuration, the heat flux profile is approximately constant until reaching the leading edge of the flame and then decreases along the streamwise coordinate [32]. The heat flux decay profile can be normalized by a characteristic length scale to follow a self-similar decay function. Therefore, if the decay function is known, the heat flux distribution can be quantified simply by means of a characteristic heat flux and a characteristic length. The characteristic heat flux

and length are chosen as the maximum heat flux and the pyrolysis length, respectively. The preheat length is then taken as the distance from the edge of the burning fuel to the location where the heat flux descends to a threshold heat flux as 11 kW/m² below which pre-heating is deemed to be negligible.

2.3 Numerical model

The numerical model performs a two-dimensional simulation based on OpenFOAM that uses a SIMPLE algorithm to solve the continuity, momentum, energy, and species equations [33]. The conservation equations are discretised on a non-uniform Cartesian grid by finite volume procedures with a first order implicit Euler scheme for time integration. The divergence terms are approximated from the second order Gauss integral scheme with limited linear interpolation; no further turbulence model is applied. For simplicity, the energy equations do not consider radiation. The absence of radiative modelling prevents direct and accurate numerical prediction of flame spread, but it is assumed that assimilation will manage to absorb the associated errors. This will be further verified in Section 3.2. The species equations are solved for the fuel taken as methyl methacrylate (MMA), oxygen, carbon dioxide, and water vapour; and the combustion model uses infinitely fast chemistry with a one-step Arrhenius reaction. Thermal properties are extracted from the NIST database [34].

The computational domain covers 0.3 m (x) × 0.03 m (y), and is divided into 80 (x) × 8 (y) cells in a non-uniform grid as fine as 1.25 mm × 1.25 mm. The flame leading edge position is fixed during the computation. The domain is designed to fully observe the flame trailing edge, so all species are gradient free at the inlet and outlet. The finest grid resolution is located close to the fuel surface to capture the flame leading edge, since flame stabilization in this region may affect combustion. This resolution is consistent with stand-off distances relevant to the present study [35], yet only requires a reduced number of cells for fast resolution. Ambient flow velocity, pressure, and oxygen content away

from the flame are adjusted in accordance with the conditions studied.

Following the principles illustrated in Figure 1, the hybrid model can be constructed, and is run both as a forward predictive model and a backward assimilation model. To trigger the forward model, initial conditions for the three regions are assigned. For the analytically described gas phase region, an initial pyrolysis length $x_{p,i}$ of 1 mm is selected, in accordance with the characteristic dimensions of a wire ignitor commonly used in related experiments. The initial flame spread rate is 0 in the analytically described condensed region, and ambient flow conditions are adopted in the CFD region.

2.4 Uncertainties from invariants in the models and data-driven implements

In both the analytical and the numerical models, there are numerous input parameters regarding thermal properties and chemical reaction coefficients which can significantly influence the results. As an illustration, Table 1 lists the input parameters required in the different regions.

Table 1 Input parameters in the hybrid model

Input parameters		
Analytical condensed phase region	Condensed Fuel thermal inertia, $k_s\rho_s c_s$	
	Condensed fuel ignition temperature, T_{ig}	
	Ambient temperature, $T_\infty = 293.15K$	
	Stoichiometric ratio, s Condensed fuel heat of gasification, $\Delta H = 25\ MJ/kg$ Condensed fuel heat of combustion, $L = 1600J/g$ Heat conductivity of the gas, $k_g = 0.159\ W(m{\cdot}K)$ Heat capacity of the gas, $c_{pg} = 2400\ J/(kg{\cdot}K)$ Ambient density of the gas, $\rho_\infty = 1.2\ kg/m^3$ Ambient oxygen fraction, $Y_{O,\infty} = 0.23$ Thickness of the analytical gas phase region, δ_a	Analytical gas phase region
CFD model	Mesh size Chemical reaction coefficients Thermal properties of species Ambient oxygen fraction, $Y_{O,\infty} = 0.23$ Ambient temperature, $T_\infty = 293.15K$ Ambient velocity, $U_\infty = 0.2m/s$	

Values for the solid thermal inertia $k_s\rho_s c_s$, consisting of thermal conductivity k_s, heat capacity c_s and density ρ_s reported in the literature can be quite different. Contrasting values provided by several studies [36–38] with direct evaluation of the thermal inertia by different groups

[39–41], the thermal inertia of PMMA approximately ranges from 0.4 to 2.55 $kJ^2/(m^4 \cdot s \cdot K^2)$. There are also some discrepancies on the characteristic ignition temperature for PMMA in the literature, which ranges from 260 to 400℃ according to different studies with various sample configurations [41–44].

Another parameter bringing significant uncertainty is the stoichiometric ratio. For complete combustion of MMA in air, the stoichiometric ratio is $s = 0.52$. However, it should be noted that, in the present configuration, combustion is not complete since quenching will always occur at the fuel surface. As such, the global mass stoichiometric ratio will always be less than 0.52. The definition of the Spalding *B* number provides the lower boundary of s below which combustion cannot happen

$$s > c_{pg}(T_{ig} - T_\infty) \big/ \Delta H_c Y_{O,\infty} \tag{8}$$

Depending on the value of the ignition temperature, s is then superior to 0.17 for an ignition temperature of 400°C, or to 0.11 for an ignition temperature of 260°C. Bering in mind this variability, the impact of the chosen values for the solid thermal inertia, the ignition temperature, and the stoichiometric ratio on the quality of the prediction is carefully assessed in Section 3.2.

Apart from these three parameters, additional inputs include a heat of gasification of 1600 J/g [35,36], heat of combustion of 25 MJ/kg [14,45], solid heat capacity and conductivity which are approximated as 2400 J/(kg·K) and 0.159 W(m·K), respectively [24]. The ambient temperature is taken as 20℃, the gas density 1.2 kg/m^3, and the ambient oxygen fraction is 0.23 in mass. In the CFD model, the infinitely fast chemistry model does not consider the detailed chemical steps and the associated kinetic coefficients. However, in a flame spread configuration, the specific chemical paths have relatively little impact on the final flame spread which is dominated by thermal effects heavily dependent on the thermal inertia, the ignition temperature, and the stoichiometric ratio.

In order to curb the uncertainties in the hybrid model, predictions are made through data assimilation by updating the inputs to synchronize the simulated results and the observations. Yet, for corrective parameters to enable a prediction, they have to be time-independent. If the parameters are time-dependent, then the model will never produce a prediction because the parameters will only be a local fit in time and therefore uncertainties beyond the data assimilation window can never be reduced. It is important to note that this is a key aspect of all data assimilation approaches that needs to be carefully assessed here.

The convergence of the assimilated variables can be used to identify the assimilation time required for proper predictions. A criterion is proposed by comparing the updated and previous assimilated variables at each of the considered time steps. Based on the relative differences between the updated assimilated variable, $C_{i,updated}$, and previous assimilated variable, $C_{i,previous}$, the convergence criteria index ε is calculated for N types of assimilated variables as,

$$\varepsilon \le max\left\{\frac{\left|C_{i,updated}-C_{i,previous}\right|}{C_{i,updated}}\right\}, i=1,2,...,N \tag{9}$$

The choices of the number and nature of the assimilate variables are critical. Numerous parameters can be assimilated if the forward model incorporates sufficient details of the physical and chemical processes. Nevertheless, increasing the number of parameters is not necessary because the desired output is not equally sensitive to all the potential parameters. In addition, more parameters means more dimensions to solve and more independent types of data that need to be assimilated, hence additional computational time and the potential for internal compensation between assimilation variables arise.

For the concurrent flame spread, the condensed and gas phases have different characteristic

timescales. The properties of the condensed phase change at a slower pace than those of the gas phase, which means that parameters change in the gas phase only slowly affect the condensed phase. Following previous work for the droplet combustion [16], two parameters representing the condensed phase and the gas phase, respectively, are chosen to be assimilated to the forward model. In the condensed phase, the parameter $\boldsymbol{C_1}$ is introduced in Eq. (7) to tune the ignition delay time described in Eq. (7), delivering:

$$t_{ig} = \boldsymbol{C_1} \frac{\pi}{4} k_s \rho_s c_s \left(\frac{T_p - T_\infty}{\dot{q}''_e} \right)^2 \tag{10}$$

Then, amending the properties of the gas phase through the mass transfer number B is an attractive option since this dimensionless number is the ratio between the heat received from the flame and the heat transferred at the fuel surface. Introducing an assimilation variable can thus correct the heat losses at the fuel surface from the observations, and absorb the uncertainties related to the radiative balance with a direct impact on the species mass fraction, temperature, the velocity field, and eventually the flame spread rate. Further detailing Eqs. (4) and (5), the mass flux at the fuel surface is defined as

$$\dot{m}''(x) = -\frac{1}{2} f(0) \rho_\infty U_\infty \left(\frac{\rho_\infty U_\infty}{\nu} x \right)^{-\frac{1}{2}} \tag{11}$$

with ρ_∞ the density of ambient air, U_∞ the velocity of the forced convective flow, ν the kinetic viscosity. In Eq.(5), the heat loss at the solid surface $\dot{q}''_{\mathrm{L}}$ consists of surface reradiation, flame radiation, in-depth conduction and any other radive inputs. For the purpose of this model, $\dot{q}''_{\mathrm{L}}$ will be assumed to be independent of x [29]. Since errors are likely to arise from the ratio of Eq. (5), a second assimilation variable $\boldsymbol{C_2}$ is adopted to correct the Spalding B number through Q:

$$Q = \frac{\dot{q}''_L}{\dot{m}''(x)} = \boldsymbol{C_2} x^{\frac{1}{2}} \tag{12}$$

where the $x^{\frac{1}{2}}$ dependency stems from the analytical solution to the local burning rate. As the flame starts to propagate, the flame radiation rapidly reach a steady value. In contrast, the solid radiative heat losses may not attained a steady-state value as fast because of the thermal inertia. Consequently, the assumption that C_2 is a constant is likely not appropriate at the beginning of the fire growth stage while $\dot{q}''_{\mathrm{L}}$ is changing.

Both C_1 and C_2 are calibrated through inverse process. To that end, a gradient descent algorithm is implemented with a cost function corresponding to the root mean square error (RMSE) between the predicted and the observed pyrolysis length. The corrected parameters C_1 and C_2 then minimize the cost function, with a cut-off criterion once the RMSE falls below 1mm. The initial guesses of C_1 and C_2 are necessary for the assimilation, and their impact on the final result is quantified by testing several combinations of C_1 and C_2 ranging from 0.01 to 100 in Section 3.1.

2.5 Overall flowchart

With all the components of the models and data-driven process, the flow chart in Figure 2 summarizes the forward and inverse processes.

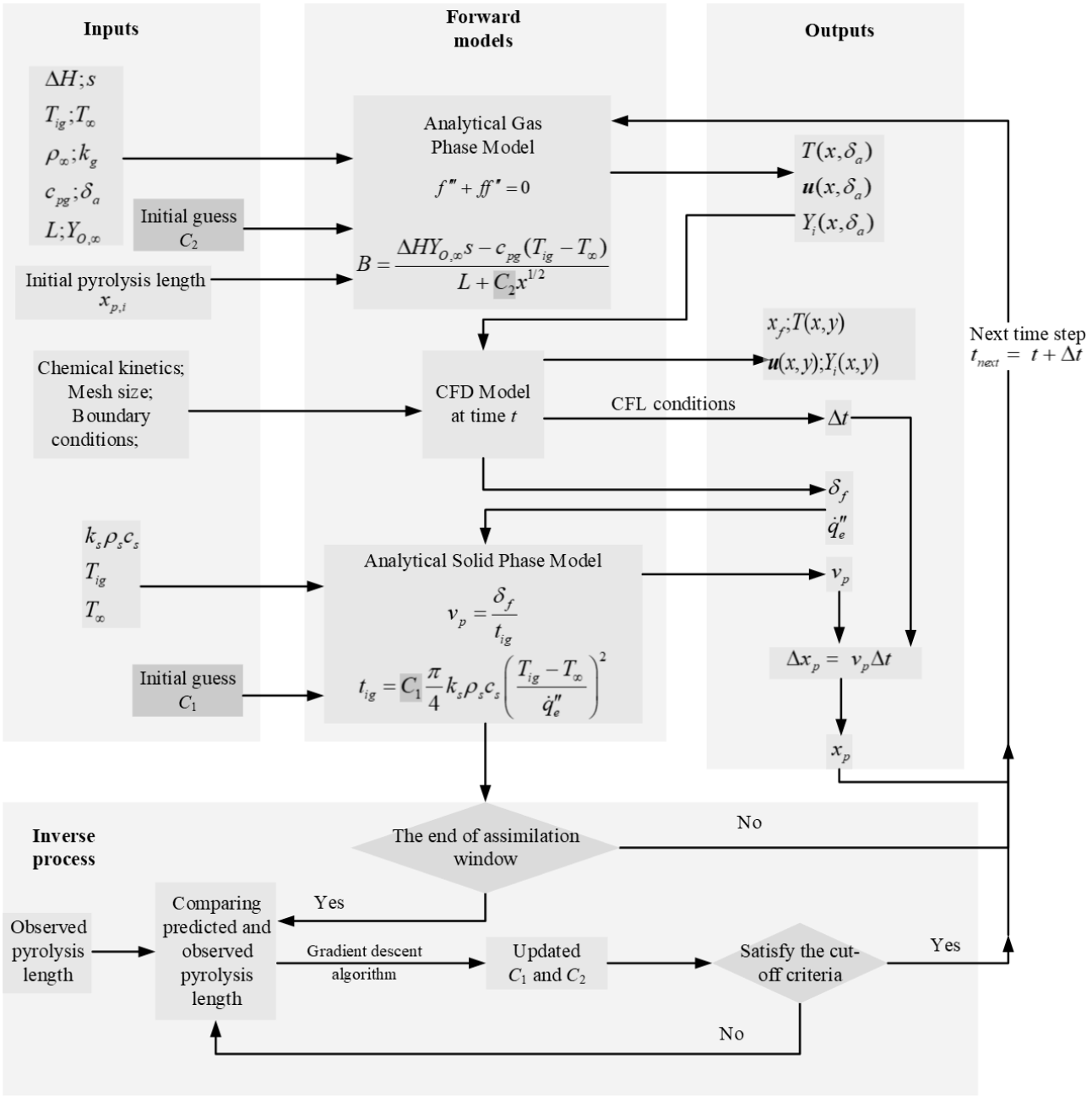

Figure 2 The flowchart shows the elements in the data-driven model. Starting from the inputs and an initial guess for C1 and C2, the forward model is first run in association with the inverse process to assimilate variables. Once assimilation is over, prediction is provided by the forward models.

Firstly, the invariants and the initial guess of the assimilation variable C_1 in the analytically described gas phase region are taken to calculate the properties at the interface between the analytical

gas phase region and the CFD region. Then the CFD model is deployed together with other associated initial and boundary conditions. By obtaining the heat flux distribution from the CFD region at the interface, the flame front velocity v_p can be evaluated in the analytically described condensed phase region with the initial guess of the assimilation variable C_2 and other invariants. Meanwhile, the CFD model also provides the numerical time step Δt. The increased pyrolysis length Δx_p then becomes $\Delta x_p = v_p \Delta t$. The evolution of the pyrolysis length is recorded in a cumulative manner by summation of the increments. The processes are repeated at the next time step $t_{next} = t + \Delta t$. At the end of the data assimilation window, the predicted and observed pyrolysis length evolutions up to that timestep are compared, and C_1 and C_2 are updated in the inverse process through gradient descent algorithm iteratively until the cut-off error criterion is satisfied. With the updated C_1 and C_2, the forward models are then used for prediction until the end of the desired period.

2.6 Boundary conditions

Computations for each domain requires inputs from the other domain, as shown in Figure 3. At a set time *t*, and given both the heat flux at the fuel surface $\dot{q}''_e$ and the preheat length δ_f from the CFD model at the previous time step, the analytical description of the condensed region provides the pyrolysis length x_p from Eq.(6). Subsequently, the analytical gas phase region yields species Y_i, temperature *T,* and velocity ***u***, at the interface with the CFD region, where they are used as inputs. The CFD model then provides closure by delivering the heat flux distribution at the interface with the analytically described gas phase. The preheat length is measured from the pre-defined pyrolysis front to the location where the computed heat flux reaches the threshold value of 11kW/m^2, as discussed before. The maximum heat flux over that region, $\dot{q}''_{max}$, is then used as the characteristic heat flux for the ignition time of the unburnt region. Given the maximum heat flux and the preheat length, the flame

spread rate is obtained through the condensed model with Eq. (6) and Eq. (7), which are in turn two necessary inputs for the analytically described condensed phase. The increase in the pyrolysis region at the next time step is finally the product of the calculated flame spread rate and the time step from the CFD model. Overall, the dynamic evolution of the system is then captured through constant interactions between the three models.

It is important to note that any preheating occurring below the arbitrary threshold will result in an increase in the ambient temperature included in Equation (11), T_∞. It is expected that the constant $\boldsymbol{C_1}$ will serve to correct for this error as well as the other uncertainties described above.

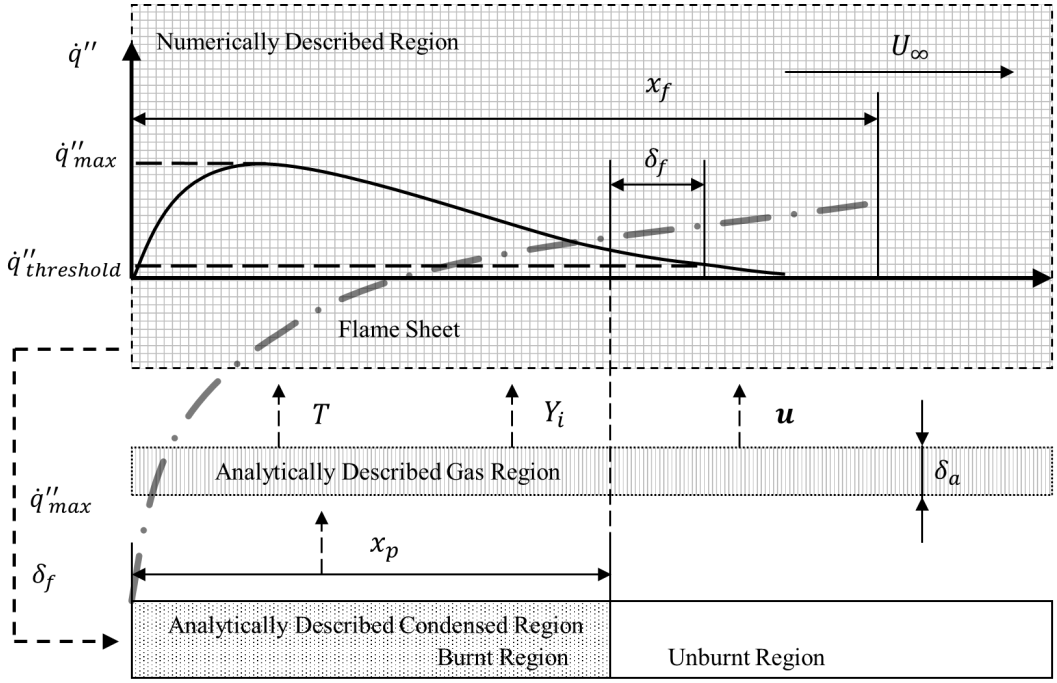

Figure 3 Flowchart of the boundary conditions and parameters at the interfaces of different regions. The heat flux distribution from the numerical model is plotted on top, to show the cut-off criterion on the right hand side of δ_f and the maximum heat flux used to compute the flame spread rate in the analytically described condensed region.

The hybrid model has limitations caused by the assumptions related to the analytical and

numerical sub-models. Ignoring radiative heat transfer underestimates both the heat feedback from the flame to the fuel surface and the radiative losses from the fuel surface. Since the balance between the two mechanisms is unclear, the uncertainty increases. Discrepancies between the analytical model and actual concurrent flame spread in microgravity exist. The radiation losses lead to the low flame temperature, which makes the gas reaction rate for the low velocity microgravity flow is slow, contradict to the infinitely fast chemistry model utilized in the analytical model. Meanwhile, a lower pyrolyzate mass flux due to the low flame temperature and flame moving away from the surface results to the changing of the flame spread rate and flame shape[23,46]. The infinitely fast chemistry combustion model therefore overestimates the temperature of the flame, resulting in a higher convective heat flux, flame spread rate and flame length. Such effect will appear and be discussed in Section 3.3. The numerical model is also sensitive to the initial and boundary conditions, meaning that the initial steady-state errors can propagate through the time and space. However, the associated error varies slowly in time so the definition of the two assimilated variables is such that these effects can be assimilated in the hybrid model.

2.7 Experimental observations

A large-scale experiment was performed in Saffire-IV [47] where concurrent flame spread over a flat PMMA sample in microgravity was investigated. In this experiment, the 0.4-m-wide, 0.18-m-long, and 0.01-m-thick PMMA fuel sample is ignited in a 0.2 m/s flow parallel to the sample surface. The flow is made of 22% oxygen and 79% nitrogen in volume, at a pressure of 1 atm. Following a 60s ignition period using a hot wire, the flame is free to spread and grow for 580s before the flow velocity is turned down. Thermocouples, radiometers, gas analysers, and three-colour cameras recoded the spread. A flashing illumination allowed visualisation of the fuel surface every 2s, providing access to

the pyrolysis length. Since this work aims at providing fire spread predictions in situations where detailed diagnostics such as radiometers or thermocouples may not be available, data were primarily extracted from the camera images. Through the experiment, the pyrolysis and flame lengths are extracted but measurements are restricted to the central 1/3 of the sample width to minimize edge effects. The pyrolysis length is considered for both data assimilation and prediction validation, while flame length serves as prediction validation only, to assess internal compensation and the transverse nature of the prediction.

Assuming that the degradation corresponds to a darkening of the fuel surface, the pyrolysis length is captured manually from illuminated frames along the central axis. The flame length is measured through the threshold images from the RGB images. The blue channel is interrogated to capture the emission from both soot particles and CH radicals. Summing pixel intensities of a top-view camera in the direction perpendicular to the flame spread axis, an average intensity curve is available at each timestep. The flame front positions are then captured from the average intensity curve by setting threshold values. The threshold values are carefully varied according to the camera gain evolution, to always capture the same flame spontaneous emission intensity.

3. Results

3.1 Convergence of the assimilated parameters

Data assimilation with different assimilation periods is conducted to investigate the time-dependency. Observations of the pyrolysis length are compared with the model outputs directly without averaging or smoothing. Data assimilation is then performed over five different periods of observations, namely [0s, 100s], [0s, 200s], [0, 300s], [0s, 400s], and [0s, 500s]. For each assimilation

window, the inverse algorithm is implemented to find the corresponding C_1 and C_2. Though C_1 and C_2 should be continuously updated every time a new data point is assimilated, the comparison is only performed over these five periods of assimilation for simplicity. Concomitantly, the influence of the initial values of C_1 and C_2 is also investigated to assess the robustness of the process, starting from 0.01, 10, 30, and 100, respectively. The resulting values of C_1 and C_2 are plotted in Figure 4. As can be seen in the figure, C_1 and C_2 evolve rapidly through the first 0~100s assimilation period and, as more data points are considered, C_1 and C_2 rapidly converge, regardless of the initial choice. This systematic convergence implies that the data assimilation model is robust, and proper predictions can be made available with time-independent assimilated variables. The reason for taking 30 as the initial value is that the cases with initial values as 0.01 and 10 both for C_1 and C_2 have ascending convergence tendencies. The case with the initial value of 30 together with the initial value as 100 provide examples with descending convergence tendencies.

Dele

It should be noted that the converged values from different initial guesses are not exactly the same as shown in the top-right insert of Figure 4, and with a higher assimilated value of C_1 the corresponding assimilated value of C_2 is lower. That is because the precision range of the convergence criterion for assimilation tolerates a range of solutions due to possible compensation mechanisms. Yet, all resulting combinations forecast the same pyrolysis length within the acceptable precision. The evolution of this system thus can be predicted properly.

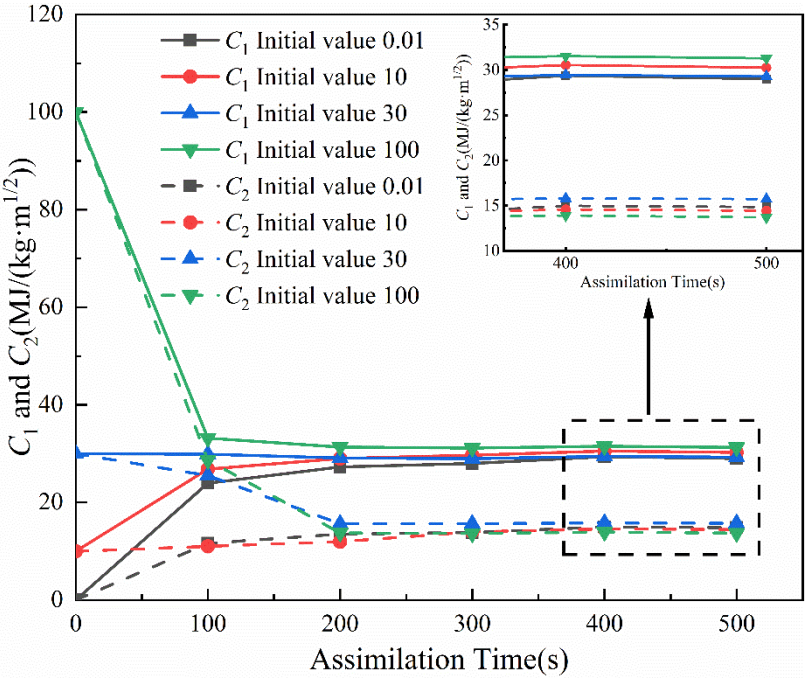

Figure 4 Assimilated C_1 and C_2 with different assimilation time from different initial guesses. The solid lines represent the evolution of C_1 with the assimilation time and the dashed lines represent the evolution of C_2 with the assimilation time. The top right insert shows the zoomed-in assimilated values for large assimilation periods.

Figure 5 shows how the error index, ε, changes with the assimilation periods. A threshold is set on ε to identify the necessary assimilation time, and results for a 10% variation ($\varepsilon = 0.1$) and a 5% variation ($\varepsilon = 0.05$) are presented in Figure 5. With a threshold of 0.1, initial values of 0.01, 30 and 100 will be assimilated properly with 300s assimilation period, while the initial values of 10 requires 400s. With a lower threshold of 0.05, the necessary assimilation time remains as 300s for initial values of 30, and 100, while it requires all of the 500s of observation for an initial guess of 0.01 and 10. Non-monotonic trends are visible in Figure 5, due to the nonlinearity of the model and potentially to the uncertainties in the observations [48]. The uncertainties are produced by the cutoff criteria of the inverse algorithm, the observational errors, and assumptions in the forward model. Overall, the

convergence criteria declines for all four cases. Therefore, it can be established that convergence is systematically attained.

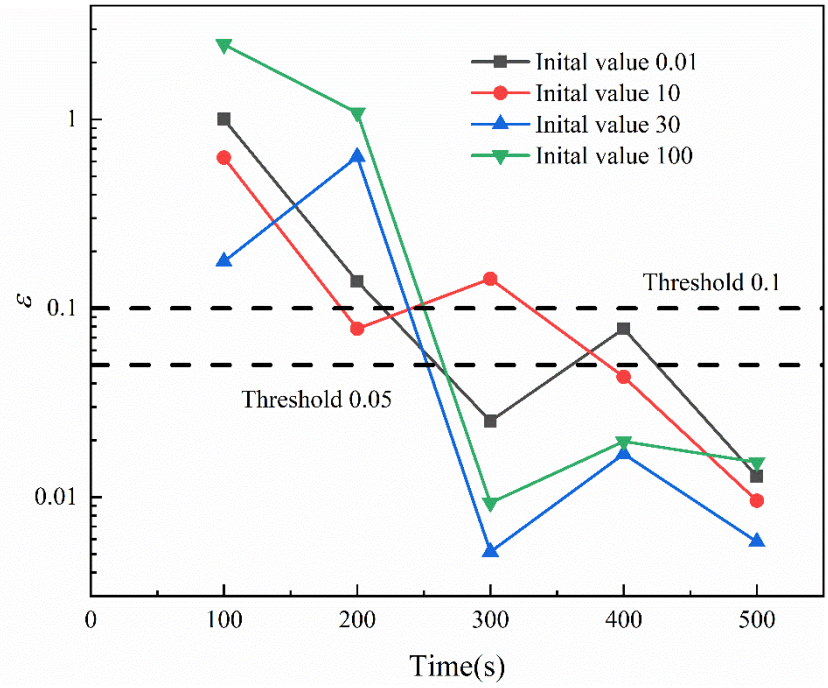

Figure 5 Convergence criteria index changing with different assimilation time from different initial guesses of 0.01 (black), 10 (red), 30 (blue) and 100 (green). Two thresholds values of 0.1 and 0.05 are specified in black dotted lines to identify the necessary assimilation time.

3.2 Influence of model parameters

The final values of C_1 and C_2 are indeed influenced by the values of the input invariants. The influence of the thermal inertia, the ignition temperature, and the stoichiometric ratio on the prediction is now quantified, because these parameters have relatively large uncertainties as described in Section 2.4. From Section 2.4, the thermal inertia ranges from 0.4 $kJ^2/(m^4 \cdot s \cdot K^2)$ to 2.66 $kJ^2/(m^4 \cdot s \cdot K^2)$, the ignition temperature ranges from 260 °C to 400 °C, and the stoichiometric ratio from 0.11 to 0.52 or from 0.17 to 0.52 for ignition temperatures of 260 °C or 400 °C, respectively. Critical stoichiometric

ratios exist below which the forward model cannot describe the observations (see Figure 6). For the ignition temperature of 260 ℃, the critical stoichiometric ratio is found around 0.16 and for the ignition temperature of 400 ℃, the critical stoichiometric ratio is about 0.18. Stoichiometric ratios slightly above their minimum values are then implemented to show the influences of the stoichiometry on convergence, using 0.18 for an ignition temperature of 260 ℃ and 0.2 for an ignition temperature of 400°C. In both cases, the maximum stoichiometric ratio is 0.52 for the completed combustion. Using these extreme values, eight converged cases featuring different thermal inertia, ignition temperature and stoichiometric ratio are assimilated, with an initial guess of 100 for C_1 and C_2 and a convergence criterion $\varepsilon = 0.1$. Table 2 shows the assimilated C_1 and C_2 obtained with different input invariants through 500s of assimilation time. The standard deviation of the observation fluctuations is 2.09 mm. The maximum observation period is used for assimilation to illustrate how data assimilation can make the forward model outputs approach the observations independently of the choice of the various static input parameters. With the adjusted assimilated variables, the pyrolysis length can be estimated as shown in Figure 6.

Table 2 Assimilation variables with different input static parameters

Case	Thermal inertia $kJ^2/(m^4 \cdot s \cdot K^2)$	Ignition temperature ℃	Stoichiometric ratio	C_1	C_2 $MJ/(kg \cdot m^{1/2})$	RMSE mm
1	0.4	260°C	0.18	1.38	5.17	0.21
2	0.4	260°C	0.52	31.47	13.25	0.47
3	0.4	400°C	0.2	13.10	2.37	0.22
4	0.4	400°C	0.52	12.21	16.93	0.17
5	2.55	260°C	0.18	0.23	4.72	0.32
6	2.55	260°C	0.52	4.78	13.24	0.46
7	2.55	400°C	0.2	1.32	1.61	0.21
8	2.55	400°C	0.52	1.96	17.06	0.17

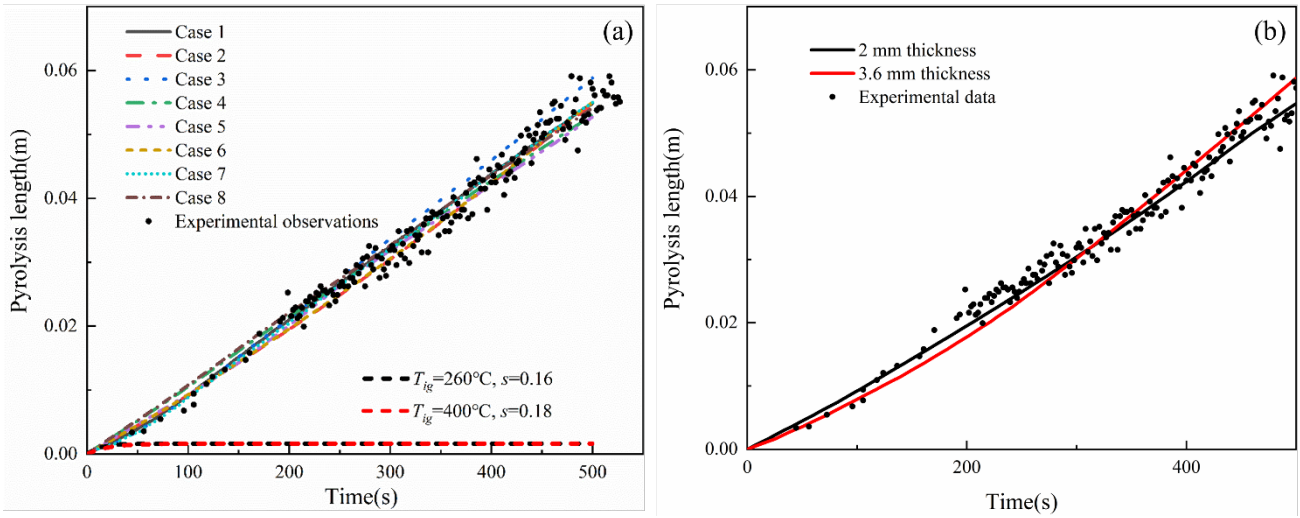

Figure 6 Assimilated pyrolysis length with different input invariants. Lines show the pyrolysis length by adjusting the assimilated variables. Dots represent the experimental pyrolysis length. (a) assimilated pyrolysis length with different thermal inertia, ignition temperature and stoichiometric ratio; including two cases where the stoichiometric ratio was too low for the model to attain a proper prediction (thick red and black dash lines). (b) assimilated pyrolysis length with different thickness of the analytically described gas phase region.

From Figure 6(a), it can be seen that most assimilated pyrolysis lengths with different input invariants provide pyrolysis length predictions with an accuracy within the experimental uncertainty. As a consequence, assimilations can be conducted properly for a wide range of accepted values for the different input parameters. The remaining differences between cases account for the cut-off criteria of the inverse algorithm. As listed in the Table 2, the RMSE is different and the pyrolysis lengths calculated can slightly differ.

Yet, C_1 and C_2 are not properly assimilated in cases when the stoichiometric ratio is lower than

the critical values. Two additional cases show the evolution of the pyrolysis length with stoichiometric ratios of 0.16 and 0.18, for ignition temperatures of 260°C and 400°C, respectively, and a thermal inertia of 0.4 $kJ^2/(m^4 \cdot s \cdot K^2)$. In both cases, the pyrolysis length initially increases for a short period of time, but then reaches a plateau, and assimilation fails to deliver the correct pyrolysis length. At such low stoichiometric ratio, little fuel is released from the combustible surface, and the flame generated above the surface will also be small. Because the subsequent preheat length is smaller than the mesh size, the preheat length becomes effectively zero and the pyrolysis length reaches a plateau. Though worth noticing, this situation is limited to the stoichiometric ratio with no physical meaning: as far as meaningful values are adopted, the performance of the predictive model is not affected by the exact value of *s*.

Another artificial parameter that deserves attention is the thickness of the analytical gas phase region, which is a portion of the boundary layer. The viscous layer thickness can be calculated from wall y^+ approach as $y^+ = (uy/\nu)$ [49]. By setting the characteristic velocity as ambient velocity, kinetic viscosity ν as 1.48×10^{-5} m/s^2, the thickness of the viscous layer is approximated as 2 mm as y^+ is chosen as 30 [49,50]. Alternatively, the laminar viscous boundary layer can also be approximated as $\delta_a \sim (\nu L/U_\infty)^{1/2}$ [51]. With this approach, a thickness of 3.6 mm is found extracting a characteristic length L = 0.4 m from the sample width. With a thermal inertia of 0.4 $kJ^2/(m^4 \cdot s \cdot K^2)$, an ignition temperature of 260 ℃ and a stoichiometric ratio of 0.52, Figure 6(b) shows the assimilated pyrolysis lengths obtained for both thicknesses. In both cases, the assimilated pyrolysis length is in agreement with the experimental observations, which indicates that the assimilation model is still valid with different thicknesses of the analytical gas phase region, as long as the flame remains within the CFD region.

3.3 Predictions for concurrent flame spread over PMMA

Figure 7 shows the experimental and predicted pyrolysis length for an ignition temperature of 260°C, a thermal inertia of 0.4 $kJ^2/(m^4 \cdot s \cdot K^2)$, and a stoichiometric ratio of 0.52. By setting the convergence criteria index ε as 0.1, 300s assimilation is sufficient for the predictions as discussed in Section 3.1. As illustrated in Figure 7, the calibration of C_1 and C_2 over the 300s provides an adequate prediction of the evolution of the pyrolysis length over the remaining sequence, with no significant deviation from the experimental data.

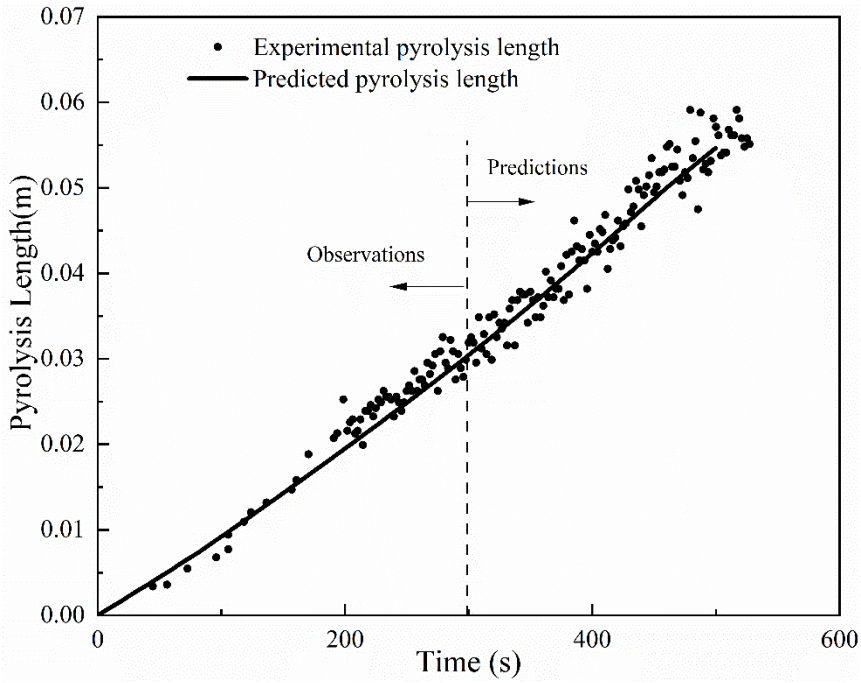

Figure 7 Evolution of the pyrolysis length for a concurrent flame spreading over PMMA in microgravity. Data assimilation is performed during the first 300s. Black dots represent the experimental data, the solid line shows prediction from a two-parameters assimilation up to 300s (dotted line).

The results from the methodology are not limited to the geometric measurements. A clear

improvement from the work of Cowlard et al [17] is that many other variables can be extracted from the predictions of this model once the assimilation period is complete. A critical variable for fire safety, shown on Figure 8 for different time steps, is the heat flux distribution at the fuel surface. The heat flux peaks above the pyrolysis region and then decreases. The approximation that the hybrid model excludes the radiative heat flux will bring errors into the model and the assimilation processes can correct such effects. The heat flux distributions are similar to each other at different time, justifying that the maximum heat flux can characterize the overall distribution. The black dash line shows the threshold value as the critical heat flux used. From the threshold value, the preheat length can be obtained.

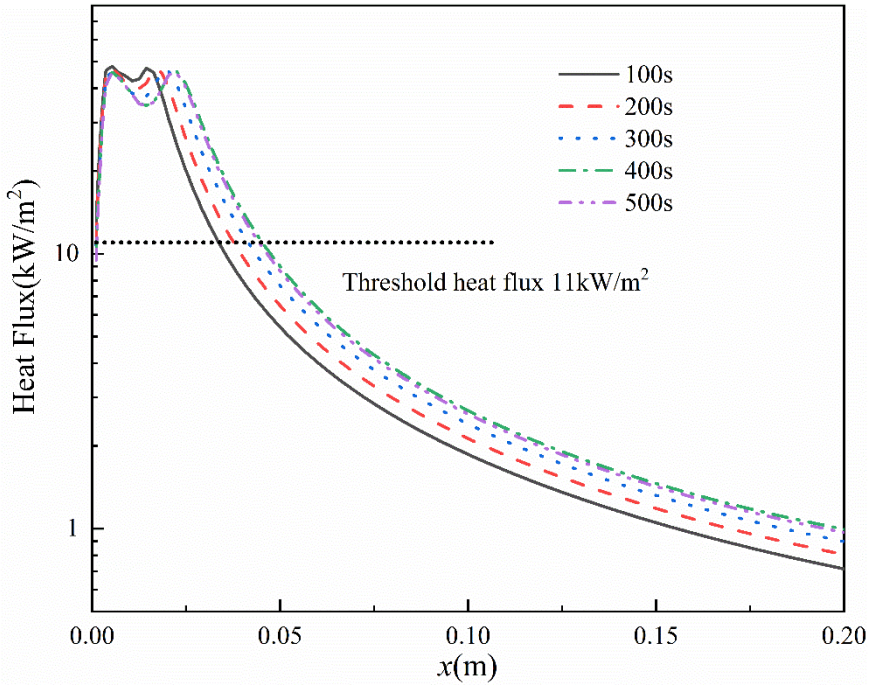

Figure 8 Computed heat flux distributions at the interface between the numerical and analytical gas regions, for different times. The dotted line represents the threshold value of 11kW/m^2 used for the critical heat flux.

In order to expand the predictions to other flame parameters, flame length measurements, which

are not assimilated, are also contrasted with predictions. Figure 9 reports the evolution of flame length in time. In the numerical model, the flame length is assumed to correspond to the maximum streamwise distance where the fuel mass fraction is above 0.05 locally. Because of the infinitely fast chemistry model, this definition of the flame length is fairly insensitive to the value of the threshold [52]. The discrete evolution of the predicted flame length is then a consequence of the chosen CFD grid, with a characteristic step of 2 mm in the present case. It can be seen that flame length is over-predicted in the data-assimilation period, and increases at a lower rate than is reported in the experiments, eventually leading to an under-prediction of the flame length after 250s. Overall, the flame length increase rate is always under-predicted.

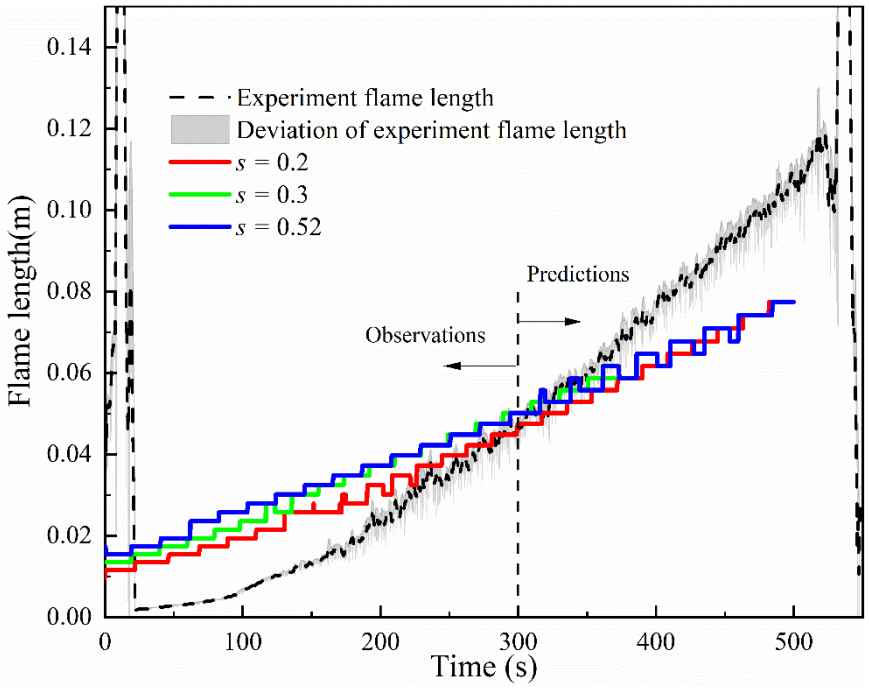

Figure 9 Evolution of the flame length for the concurrent flame spread over PMMA in microgravity. The black dotted line represents the experimental data averaged over a 2s time window, and the shadow represents the variance. Red, green, and blue solid lines show the predicted flame length for stoichiometric ratios of 0.2, 0.3, and 0.52, respectively.

Since the pyrolysis length is assimilated in the model, the flame spread rate which illustrates its variation is consistently delivered. Given the similarity of the heat flux profiles from the flame to the fuel surface, it can be assumed that the overall description of the flame in terms of heat transfer is correct. As a result, transport and chemical mechanisms are investigated to understand the discrepancy in the evolution rate between predicted and experimental flame length. Two components related to the fuel in the gas phase, namely the local pyrolysis rate from the condensed phase and fuel consumption at the trailing edge may account for the discrepancy in the flame length. In the early stage of the propagation, the model overpredicts the flame length. At that moment, the transient heat transfer into the condensed phase cannot generate stable mass burning. The quasi-steady-state assumption thus becomes invalid and the boundary conditions provided by Eq.(3) cannot work. The temperature profile in the condensed phase is smooth, while the solid is still heating up. Eventually, the heat losses from the pyrolysis gases to the cold surface are underpredicted in the model, and the position of the flame trailing edge is overestimated. As a result, the predicted flame length is over-estimated. In the later stage of the propagation, the flame length is underpredicted. Although quasi-steady-state can now be achieved, the complete combustion assumption both for the analytical described gas phase region and numerical region conflicts with the fact that the flame is quenched at the trailing edge and unburnt fuel is released. Since the global stoichiometric ratio can be interpreted as a relevant parameter describing the completeness of the combustion, its influence on the flame length is investigated. Figure 9 includes three flame spread predictions with stoichiometric ratios of 0.2, 0.3, and 0.52, respectively. In each situation, data assimilation is performed over 300s before predictions are made, meaning that three sets of constants C_1 and C_2 are extracted. The assimilation is successfully carried out for each stoichiometric ratio, but none of the predictions satisfy the experimental observations. It indicates that

the flame length cannot be predicted correctly with a constant stoichiometric ratio, no matter the adopted value.

A critical interpretation from Figure 9 is that the flame spread rate can be predicted properly while the flame length cannot be reproduced correctly. It suggests that the flame spread rate and flame length are independent variables in this situation, which is in opposition with previous models developed for vertical buoyant spread in which these two components are coupled [12,53,54].

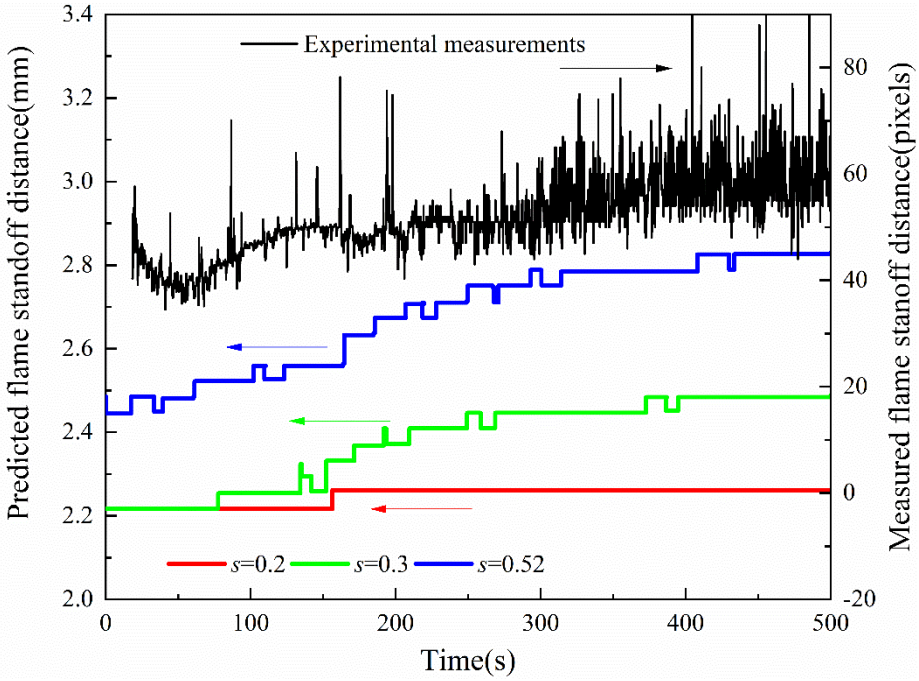

Figure 10 Evolution of the predicted and experimental flame standoff distances for the concurrent flame spread over PMMA in microgravity. The black solid line represents the experimental flame standoff distance in units of pixels. Red, green, and blue solid lines show the predicted flame standoff distance in units of millimetres for stoichiometric ratios of 0.2, 0.3, and 0.52, respectively.

The varying stoichiometric ratios associated with another assimilation variable may be capable to reproduce the flame lengths as discussed before. The flame standoff distance is directly related to the stoichiometric ratio[29]. Observations of the flame standoff distances could thus be used to

assimilate the changes in the stoichiometric ratio. Figure 10 reports the standoff distances at the flame trailing edge for different stoichiometric ratios of 0.2, 0.3, and 0.53. With a higher stoichiometric ratio, the flame standoff distance increases. The experimentally measured standoff distances at the flame trailing edge are obtained from a side-view camera. Processing the blue channel, the position of the flame is obtained using a threshold value, but conversion from pixel to distance fails because the tilt angle of the camera and the distortion induced by the lens have not been evaluated. In addition, this measurement is likely distorted by edge effects of the flame. In the present conditions, no better flame lengths can be predicted without more precise observations. Future investigations will focus on upward flame spread at normal gravity, to investigate if the missing coupling between flame length and spread rate is observed.

This methodology can still be improved in terms of computational time. The CPU time is about 10 minutes for 600s simulation of the forward models on a 1.9GHz i7-8650 CPU. The times of iterations of the inverse process can be further reduced if high performance computers with parallel computation configuration is available because several iterations can be conducted at the same time. Besides, with more sophisticated inverse algorithms, the iterations time for assimilation process can be further reduced.

4. Conclusion

The complex heat and mass coupling between the gas and condensed phase impedes the precise, valid and timely forecasts in fire. A novel framework for data driven forecasts of concurrent flame spread in microgravity, consisting of coupled analytical and numerical models, is presented. Two assimilated variables related to the gas and condensed phases, respectively, are proposed to steer the assimilation.

Capitalizing on recent large-scale experiments in microgravity, a series of simulations are performed. The robustness of the method is successfully validated through variation of initial guesses of the two assimilated variables for different assimilation windows, and fluctuations in the input invariants. Eventually, the flame spread rate can be successfully assimilated for a range of values of the different input parameters consistent with the present state of literature. The method shows that the flame spread rate can be correctly assimilated from the adjustment of the heat transfer from the gas phase to the condensed phase without providing a correct estimation of the flame length in the process. It implies that the predictions of uncorrelated gas and condensed phases could be separated at a certain level within this new methodology. While providing this extra level of complexity consistent with boundary layer flame theory, this framework can massively reduce the computational time of an all-CFD prediction, without compromising on the description of the heat transfer mechanisms, envisioning real-time forecasts.

5. References

[1] A. Cowlard, W. Jahn, C. Abecassis-Empis, G. Rein, J.L. Torero, Sensor Assisted Fire Fighting, Fire Technol. 46 (2010) 719–741. https://doi.org/10.1007/s10694-008-0069-1.

[2] J.L. Torero, Scaling-Up fire, Proc. Combust. Inst. 34 (2013) 99–124. https://doi.org/10.1016/j.proci.2012.09.007.

[3] I. Glassman, F.L. Dryer, Flame spreading across liquid fuels, Fire Saf. J. 3 (1981) 123–138. https://doi.org/10.1016/0379-7112(81)90038-2.

[4] A. Fernandez-Pello, F.A. Williams, Laminar flame spread over PMMA surfaces, Symp. Int. Combust. 15 (1975) 217–231. https://doi.org/10.1016/S0082-0784(75)80299-2.

[5] D.L. Urban, P. Ferkul, S. Olson, G.A. Ruff, J. Easton, J.S. T'ien, Y.-T.T. Liao, C. Li, C. Fernandez-Pello, J.L. Torero, G. Legros, C. Eigenbrod, N. Smirnov, O. Fujita, S. Rouvreau, B. Toth, G. Jomaas, Flame spread: Effects of microgravity and scale, Combust. Flame. 199 (2019) 168–182. https://doi.org/10.1016/j.combustflame.2018.10.012.

[6] A.C. Fernandez-Pello, Flame Spread Modeling, Combust. Sci. Technol. 39 (1984) 119–134. https://doi.org/10.1080/00102208408923786.

[7] H.W. Emmons, The Film Combustion of Liquid Fuel, ZAMM - J. Appl. Math. Mech. Z. Für Angew. Math. Mech. 36 (1956) 60–71. https://doi.org/10.1002/zamm.19560360105.

[8] J.N. De Ris, Spread of a laminar diffusion flame, Symp. Int. Combust. 12 (1969) 241–252. https://doi.org/10.1016/S0082-0784(69)80407-8.

[9] A.C. Fernandez-Pello, T. Hirano, Controlling Mechanisms of Flame Spread, Combust. Sci. Technol. 32 (1983) 1–31. https://doi.org/10.1080/00102208308923650.

[10] A. Fernández-pello, F.A. Williams, A theory of laminar flame spread over flat surfaces of solid combustibles, Combust. Flame. 28 (1977) 251–277. https://doi.org/10.1016/0010-2180(77)90032-3.

[11] L. Orloff, A.T. Modak, R.L. Alpert, Burning of large-scale vertical surfaces, Symp. Int. Combust. 16 (1977) 1345–1354. https://doi.org/10.1016/S0082-0784(77)80420-7.

[12] K. Saito, J. Quintiere, F. Williams, Upward Turbulent Flame Spread, Fire Saf. Sci. 1 (1986) 75–86. https://doi.org/10.3801/IAFSS.FSS.1-75.

[13] P.J. Pagni, T.M. Shih, Excess pyrolyzate, Symp. Int. Combust. 16 (1977) 1329–1343. https://doi.org/10.1016/S0082-0784(77)80419-0.

[14] K. Fukumoto, C. Wang, J. Wen, Large eddy simulation of upward flame spread on PMMA walls with a fully coupled fluid–solid approach, Combust. Flame. 190 (2018) 365–387. https://doi.org/10.1016/j.combustflame.2017.11.012.

[15] A. Carney, Y. Li, Y.-T. Liao, S. Olson, P. Ferkul, Concurrent-flow flame spread over thin discrete fuels in microgravity, Combust. Flame. 226 (2021) 211–221. https://doi.org/10.1016/j.combustflame.2020.12.005.

[16] Y. Li, Y.-T. Liao, P. Ferkul, Numerical Study of the Effects of Confinement On Concurrent-Flow Flame Spread in Microgravity, J. Heat Transf. 142 (2020). https://doi.org/10.1115/1.4047645.

[17] E.N. Lorenz, The predictability of a flow which possesses many scales of motion, Tellus. 21 (1969) 289–307. https://doi.org/10.1111/j.2153-3490.1969.tb00444.x.

[18] E. Kalnay, Data assimilation, in: Atmospheric Model. Data Assim. Predict., Cambridge University Press, Cambridge, 2002: pp. 136–204. https://doi.org/10.1017/CBO9780511802270.006.

[19] M. Asch, M. Bocquet, M. Nodet, Data assimilation: methods, algorithms, and applications, SIAM, Society for Industrial and Applied Mathematics, Philadelphia, 2016.

[20] C. Lautenberger, Wildland fire modeling with an Eulerian level set method and automated calibration, Fire Saf. J. 62 (2013) 289–298. https://doi.org/10.1016/j.firesaf.2013.08.014.

[21] C. Zhang, M. Rochoux, W. Tang, M. Gollner, J.-B. Filippi, A. Trouvé, Evaluation of a data-driven wildland fire spread forecast model with spatially-distributed parameter estimation in simulations of the FireFlux I field-scale experiment, Fire Saf. J. 91 (2017) 758–767. https://doi.org/10.1016/j.firesaf.2017.03.057.

[22] X. Xi, J.L. Torero, W. Jahn, Data driven forecast of droplet combustion, Proc. Combust. Inst. (2020). https://doi.org/10.1016/j.proci.2020.05.012.

[23] M. Thomsen, C. Fernandez-Pello, G.A. Ruff, D.L. Urban, Buoyancy effects on concurrent flame spread over thick PMMA, Combust. Flame. 199 (2019) 279–291. https://doi.org/10.1016/j.combustflame.2018.10.016.

[24] K. Annamalai, M. Sibulkin, Flame Spread Over Combustible Surfaces for Laminar Flow Systems Part I: Excess Fuel and Heat Flux, Combust. Sci. Technol. 19 (1979) 167–183. https://doi.org/10.1080/00102207908946878.

[25] A.C. Fernandez-Pello, Flame spread in a forward forced flow, Combust. Flame. 36 (1979) 63–78. https://doi.org/10.1016/0010-2180(79)90046-4.

[26] J.S. Kim, J. de Ris, F. William Kroesser, Laminar free-convective burning of fuel surfaces, Symp. Int. Combust. 13 (1971) 949–961. https://doi.org/10.1016/S0082-0784(71)80095-4.

[27] H.R. Baum, A. Atreya, Elliptic Solution to the Emmons Problem, in: Fire Res., University of California at San Diego, 2007: p. 17.

[28] J.L. Torero, A. Simeoni, Heat and Mass Transfer in Fires: Scaling Laws, Ignition of Solid Fuels and Application to Forest Fires, Open Thermodyn. J. 4 (2010) 145–155. https://doi.org/10.2174/1874396X01004010145.

[29] J.L. Torero, T. Vietoris, G. Legros, P. Joulain, Estimation of a total mass transfer number from the standoff distance of a spreading flame, Combust. Sci. Technol. 174 (2002) 187–203. https://doi.org/10.1080/713712953.

[30] J. Quintiere, A simplified theory for generalizing results from a radiant panel rate of flame spread apparatus, Fire Mater. 5 (1981) 52–60. https://doi.org/10.1002/fam.810050204.

[31] R.T. Long, J.L. Torero, J.G. Quintiere, A.C. Fernandez-Pello, Scale And Transport Considerations On Piloted Ignition Of Pmma, Fire Saf. Sci. 6 (2000) 567–578.

[32] J.L. Consalvi, Y. Pizzo, B. Porterie, J.L. Torero, On the flame height definition for upward flame spread, Fire Saf. J. 42 (2007) 384–392. https://doi.org/10.1016/j.firesaf.2006.12.008.

[33] H.G. Weller, G. Tabor, H. Jasak, C. Fureby, A tensorial approach to computational continuum mechanics using object-oriented techniques, Comput. Phys. 12 (1998) 620–631. https://doi.org/10.1063/1.168744.

[34] T. Allison, JANAF Thermochemical Tables, NIST Standard Reference Database 13, (1996). https://doi.org/10.18434/T42S31.

[35] A.S. Rangwala, S.G. Buckley, J.L. Torero, Analysis of the constant B-number assumption while modeling flame spread, Combust. Flame. 152 (2008) 401–414. https://doi.org/10.1016/j.combustflame.2007.09.010.

[36] J. Li, S.I. Stoliarov, Measurement of kinetics and thermodynamics of the thermal degradation for non-charring polymers, Combust. Flame. 160 (2013) 1287–1297. https://doi.org/10.1016/j.combustflame.2013.02.012.

[37] M.J. Assael, S. Botsios, K. Gialou, I.N. Metaxa, Thermal Conductivity of Polymethyl Methacrylate (PMMA) and Borosilicate Crown Glass BK7, Int. J. Thermophys. 26 (2005) 1595–1605. https://doi.org/10.1007/s10765-005-8106-5.

[38] A. Soldera, N. Metatla, A. Beaudoin, S. Said, Y. Grohens, Heat capacities of both PMMA stereomers: Comparison between atomistic simulation and experimental data, Polymer. 51 (2010) 2106–2111. https://doi.org/10.1016/j.polymer.2010.03.003.

[39] D. Hopkins, J.G. Quintiere, Material fire properties and predictions for thermoplastics, Fire Saf. J. 26 (1996) 241–268. https://doi.org/10.1016/S0379-7112(96)00033-1.

[40] Ignition of Solids, in: Fundam. Fire Phenom., John Wiley & Sons, Ltd, 2006: pp. 159–190. https://doi.org/10.1002/0470091150.ch7.

[41] H.E. Thomson, D.D. Drysdale, Flammability of plastics I: Ignition temperatures, Fire Mater. 11 (1987) 163–172. https://doi.org/10.1002/fam.810110402.

[42] T. Kashiwagi, Effects of sample orientation on radiative ignition, Combust. Flame. 44 (1982) 223–245. https://doi.org/10.1016/0010-2180(82)90075-X.

[43] J.G. Quintiere, M.F. Harkleroad, New Concepts for Measuring Flame Spread

Properties., (1984). https://www.nist.gov/publications/new-concepts-measuring-flame-spread-properties (accessed March 3, 2021).

[44] B.T. Rhodes, J.G. Quintiere, Burning rate and flame heat flux for PMMA in a cone calorimeter, Fire Saf. J. 26 (1996) 221–240. https://doi.org/10.1016/S0379-7112(96)00025-2.

[45] C.W.M. Van Der Geld, P.A.O.G. Korting, T. Wijchers, Combustion of PMMA, PE, and PS in a ramjet, Combust. Flame. 79 (1990) 299–306. https://doi.org/10.1016/0010-2180(90)90141-D.

[46] M. Thomsen, C. Fernandez-Pello, D.L. Urban, G.A. Ruff, On simulating the effect of gravity on concurrent flame spread over thin paper through variations in ambient pressure, Combust. Flame. 232 (2021) 111538. https://doi.org/10.1016/j.combustflame.2021.111538.

[47] D. Urban, G. Ruff, P. Ferkul, J. Easton, J. Owens, S. Olson, M. Meyer, C. Fortenberry, J. Brooker, J. Graf, M. Casteel, G. Jomaas, B. Toth, C. Eigenbrod, J. T'Ien, Y.-T. Liao, C. Fernandez-Pello, F. Meyer, G. Legros, A. Guibaud, N. Smirnov, O. Fujita, Fire Safety Implications of Preliminary Results from Saffire IV and V Experiments on Large Scale Spacecraft Fires, (2021). https://ttu-ir.tdl.org/handle/2346/87224 (accessed August 29, 2021).

[48] S. Arridge, P. Maass, O. Öktem, C.-B. Schönlieb, Solving inverse problems using data-driven models, Acta Numer. 28 (2019) 1–174. https://doi.org/10.1017/S0962492919000059.

[49] S.J. Kline, W.C. Reynolds, F.A. Schraub, P.W. Runstadler, The structure of turbulent boundary layers, J. Fluid Mech. 30 (1967) 741–773. https://doi.org/10.1017/S0022112067001740.

[50] J. Poggie, Compressible Turbulent Boundary Layer Simulations: Resolution Effects and Turbulence Modeling, in: 53rd AIAA Aerosp. Sci. Meet., American Institute of Aeronautics and Astronautics, Kissimmee, Florida, 2015. https://doi.org/10.2514/6.2015-1983.

[51] Laminar Boundary Layer Flow, in: Convect. Heat Transf., John Wiley & Sons, Inc., Hoboken, NJ, USA, 2013: pp. 30–95. https://doi.org/10.1002/9781118671627.ch2.

[52] T.G. Ma, J.G. Quintiere, Numerical simulation of axi-symmetric fire plumes: accuracy and limitations, Fire Saf. J. 38 (2003) 467–492. https://doi.org/10.1016/S0379-7112(02)00082-6.

[53] X. Huang, G. M.j, Correlations for Evaluation of Flame Spread over an Inclined Fuel Surface, Fire Saf. Sci. 11 (2014) 222–233.

[54] L.K. Honda, P.D. Ronney, Mechanisms of concurrent-flow flame spread over solid fuel beds, Proc. Combust. Inst. 28 (2000) 2793–2801. https://doi.org/10.1016/S0082-0784(00)80701-8.